MEDA: Measurement-Efficient Disorder-Aware Majorana Zero Mode Detection in Realistic Devices

Nathan Jones*, Binayyak Roy*, Valentine Mohaugen, Ian Lewis,
Toby Cox, Sumanta Tewari, and Rong Ge
Clemson University
Clemson, SC
{najones, binayyr, valentm, iml, tscox, stewari, rge}@clemson.edu

***Abstract*—Fault-tolerant topological quantum computing relies on identifying Majorana zero modes (MZMs), but reliable detection in realistic devices remains challenging. Conventional topological indicators become inherently biased in finite, disordered systems, blurring the distinction between true MZMs and trivial states. Furthermore, attempts to map these indicators to real observables via machine learning require dense, expensive conductance measurements, creating a severe scaling bottleneck. To simultaneously address topological bias and measurement limitations, we present MEDA: a Measurement-Efficient, Disorder-Aware framework for MZM detection in realistic devices. MEDA maps sparse, practically obtainable observables directly to the robust periodic disorder invariant (PDI). Using a novel sparse parameter regime, MEDA reduces measurement volume by 10x while maintaining predictive quality, even in moderate to strong disorder regimes that limit conventional methods. Furthermore, MEDA naturally prioritizes input features consistent with the topological gap protocol, demonstrating strong physical interpretability.**

***Index Terms*—Quantum Computing, Topological Quantum Computing, Majorana Zero Modes**

I. Introduction

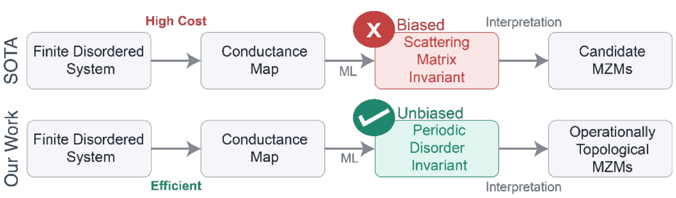

Fig. 1: **MEDA Detection Pipeline.** Unlike traditional approaches requiring dense sampling and using biased indicators, MEDA achieves scalable, bias-resilient MZM detection by mapping sparse conductance measurements directly to the disorder-aware PDI.

Topological quantum computing offers a promising route to fault tolerance by encoding quantum information nonlocally in topological degrees of freedom, suppressing sensitivity to local noise and perturbations [1]–[6]. Majorana zero modes (MZMs), non-Abelian quasiparticles predicted to emerge in topological superconductors [7]–[10], are central to this paradigm because their nonlocal nature enables fault-tolerant operations through topological braiding. However, the practical realization of this paradigm critically hinges on reliable identification of topological superconductivity in experimentally accessible, disordered devices.

Despite substantial experimental progress, robust MZM detection in realistic systems remains fundamentally challenging. Widely used topological invariants are typically derived under idealized assumptions. While successful in clean theoretical models, these tools become inherently biased [11] in finite, disordered devices, where impurities and spatial inhomogeneities blur the distinction between true topological MZMs and trivial near-zero-energy states [12]–[30].

Prior work has attempted to bridge this gap by adapting scattering matrix-based or local density of states (LDOS)-based topological indicators to finite-system settings [30]–[34]. However, these adapted indicators still inherit boundary sensitivity and disorder-related biases. Recently, the periodic disorder invariant (PDI) was proposed as a fundamentally more robust, bulk-defined topological indicator that remains well-defined in finite, disordered systems by construction [35]. Unfortunately, all of these indicators are inaccessible from experiments; they rely fundamentally on information that is unavailable outside of simulation.

To overcome this lack of observability, recent work has turned to machine learning approaches to infer topological indicators from experimentally measurable conductance data [31], [36], [37]. These methods exhibit two key limitations. First, by predicting biased indicators, they inherit the same topological shortcomings and often rely on heuristic thresholding. Second, they require densely sampled conductance maps as input. Because sweeping parameters like the chemical potential μ is an inherently serial and painstakingly slow process in physical systems [38]–[42], this dense-scanning requirement creates a severe measurement bottleneck that limits scalability. Furthermore, transitioning to a highly complex, bulk-defined PDI framework threatens to exacerbate this data-acquisition bottleneck even further.

In this work, we introduce **MEDA**, a **Measurement-Efficient, Disorder-Aware** framework designed to simultaneously address topological bias and experimental scalability, shown in Fig. 1. MEDA establishes the first direct mapping from experimentally measurable conductance data to the PDI, enabling deployment of a bulk-defined, unbiased topological diagnostic in realistic experimental settings. Crucially, MEDA

*These authors contributed equally to this work.

utilizes an attention-driven multiple instance learning (MIL) architecture that autonomously identifies the most topologically informative regions of the conductance map. MEDA breaks the dense-scanning paradigm, achieving a $10\times$ reduction in required measurement volume with high classification accuracy.

We evaluate MEDA on a comprehensive dataset of simulated one-dimensional Majorana nanowire transport observables, explicitly probing regimes with moderate to strong disorder and fragmented phase diagrams. Our main contributions are as follows:

- We propose MEDA, the first end-to-end pipeline mapping measurable conductance data directly to the binary PDI in finite, disordered semiconductor-superconductor (SM-SC) nanowires.
- We demonstrate that MEDA accurately reconstructs extended topological regions using only 10% of the original measurement volume, directly translating to massive savings in experimental acquisition time.
- We validate MEDA's generalization under realistic device conditions with moderate-to-strong disorder, where conventional indicators often fail.
- We show that the model's learned weighting naturally prioritizes physically relevant conductance features consistent with established criteria, such as the topological gap protocol.

II. Background and Motivation

A. MZMs and Topological Indicators

1) Topological Indicators: Theoretically ideal one-dimensional SM-SC nanowires can host end-localized MZMs that offer fault-tolerant quantum computing [4]. However, realistic devices deviate significantly from idealized models, making MZM presence more ambiguous. Finite-size effects allow end-states to interact, while microscopic imperfections introduce disorder that generates trivial near-zero-energy states, such as partially separated Andreev bound states (ps-ABSs) [5], [7]–[10], [12]–[21], [39], [43]–[50]. These effects jointly produce false negatives and false positives, rendering boundary-based diagnostics—including transport-based indicators [32], [40] and LDOS-based approaches [51]–[53]—intrinsically ambiguous.

The leading topological indicator for experimental systems, the scattering matrix invariant (SMI), attempts to formalize boundary-based diagnostics by characterizing topology through reflection properties of the system, ideally yielding a binary invariant [33], [54]. However, the SMI inherits the same fundamental limitations as other boundary-based indicators. Finite-size effects force continuous SMI values, and attempts to reduce false negatives via topological visibility (TV) [40], [55] amplify false positives from quasi-Majorana states [11], [27], [28], [56].

Additionally, SMI remains experimentally inaccessible despite its connection to transport. The full scattering matrix cannot be directly measured, and experimental proxies such as zero-bias conductance peaks depend sensitively on fine tuning of external measurement conditions, rather than intrinsic system topology. As a result, the SMI remains biased in realistic regimes and impractical for experimental deployment.

TABLE I: Due to its critical sensitivity to finite-size effects, disorder, and measurement tuning, the SMI cannot serve as a reliable diagnostic in real-world systems. The robust PDI must therefore serve as the ground truth, motivating our mapping approach.

Property	**SMI**	**PDI**
Theoretical Basis	Boundary scattering processes ($\det(r)$)	Bulk properties (System Hamiltonian)
Nature of Output	Continuous proxy ($-1 \leq \det(r) \leq 1$)	Strictly quantized and binary $(0, 1)$
Observability	Unobservable; relies on localized conductance proxies	Unobservable; serves as the ground-truth target for inference
Finite-Size Effects	**Vulnerable:** Hybridization causes false negatives	**Robust:** Inherently accounts for finite nanowire length
Microscopic Disorder	**Vulnerable:** Quasi-MZMs induce severe false positives	**Robust:** Accurately incorporates the full disorder profile
Measurement Tuning	**Vulnerable:** Requires fine-tuning of external lead coupling	**Robust:** Independent of external measurement artifacts

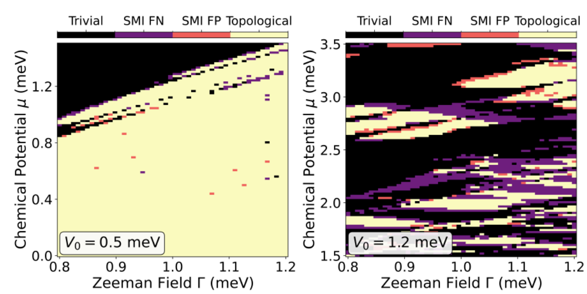

Fig. 2: While SMI performs comparatively well under weaker disorder (e.g., $V_0 = 0.5$ meV), it produces significant false detections under moderate disorder (e.g., $V_0 = 1.2$ meV) when compared to PDI.

2) Periodic Disorder Invariant (PDI): In contrast, the PDI [11], [35] provides a bulk-defined, unbiased diagnostic. Constructed by embedding the finite disordered nanowire into an infinite superlattice, the PDI yields a strictly quantized binary invariant that natively incorporates the full microscopic disorder profile. By eliminating boundary sensitivity, the PDI remains robust against finite-size effects, correcting SMI misclassifications, as shown in Fig. 2. Table I summarizes PDI's advantages over SMI.

B. Experimental Bottlenecks and Motivation

While the PDI is theoretically robust, its reliance on the full system Hamiltonian prevents direct experimental deployment. Instead, experimentalists rely on boundary observables, such as differential conductance, measured over an extended parameter space that includes both control parameters and measurement variables. This creates a fundamental challenge:

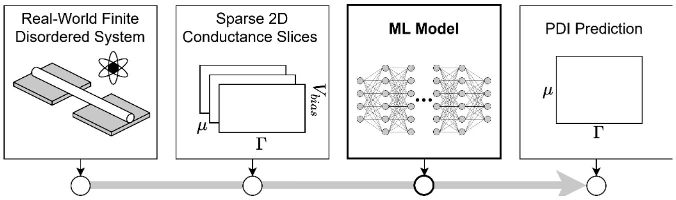

Fig. 3: MEDA provides a scalable, bias-resilient pipeline for MZM detection for real-world devices by mapping sparsely sampled conductance measurements to the disorder-aware PDI.

inferring bulk topology—and consequently the underlying phase diagram—from indirect, measurement-dependent observables.

Real-world measurement of these observables presents a severe bottleneck. Extracting conductance signals in a dilution refrigerator is a slow and serial process that requires millisecond-scale integration time per measurement point [57]. Sweeping the chemical potential (μ) axis is particularly costly due to charge trap dynamics, cross-capacitance compensation, and electrostatic relaxation delays [38]–[40]. As a result, reconstructing a high-resolution phase diagram is prohibitively expensive [41], [42]. While traditional methods circumvent this by densely sampling a narrow parameter window, we propose an inverted paradigm: expanding parameter exploration within a fixed budget by strategically subsampling conductance data, particularly along the costly μ axis.

III. MEDA Framework

MEDA formulates the translation of sparse experimental observables into a bulk-defined topological invariant as an end-to-end supervised machine learning inference task, as shown in Fig. 3. By leveraging a data-driven architecture, MEDA maps non-local transport signatures directly to the PDI.

A. Machine Learning Abstraction

Input Space ($\mathcal{X}$): The input $X \in \mathcal{X}$ is a sparsely sampled "bag" of k discrete multi-channel differential conductance slices sampled across the chemical potential μ, denoted as $X = \{X_1, X_2, \ldots, X_k\}$. While MEDA supports an arbitrary measurement budget k, we utilize $k = 10$ throughout this work as the optimal trade-off between experimental feasibility and predictive accuracy, as detailed in Section V. Deliberately subsampling along the μ axis vastly expands the explorable parameter volume for a given measurement budget. Each slice $X_i \in \mathbb{R}^{N_{V_{bias}} \times N_\Gamma \times C}$ is a 3rd-order tensor representing a 2D spatial grid over the bias voltage V_{bias} and the Zeeman field Γ, with a channel depth of $C = 4$. The feature depth corresponds to the measurable local and non-local differential conductance channels: $(G_{LL}, G_{LR}, G_{RL}, G_{RR})$.

Output Space ($\mathcal{Y}$): The target output $Y \in \{0,1\}^{N_\mu \times N_\Gamma}$ is a high-resolution, binary grid representing the system's ground-truth topological state, dictated by the PDI phase map over the full (μ, Γ) parameter space. While PDI is unaffected by V_{bias}, it changes sharply with μ. Thus, we use the fully dense μ axis for the PDI map rather than the sparse μ input. A value of 1 indicates a disorder-resilient, operationally topological MZM phase, while 0 indicates a trivial state.

Mapping and Objective (f_θ): We aim to learn a parameterized mapping f_θ that transforms the sparse input observables into a probability phase map:

$$f_\theta : \mathbb{R}^{k \times N_{V_{bias}} \times N_\Gamma \times 4} \to [0,1]^{N_\mu \times N_\Gamma}$$

where $\hat{Y} = f_\theta(X)$. Each element $\hat{Y}_{i,j}$ represents the model's predicted probability that the physical device exists in a topologically non-trivial state at the specific physical coordinates (μ_i, Γ_j). The neural network is optimized to minimize the discrepancy between the continuous prediction $\hat{Y}$ and the binary ground truth Y, yielding a surrogate model capable of inferring a global, bulk-defined topological invariant from partial surface observables without requiring full microscopic observability.

1) Input Representation: We abstract the multi-channel conductance slices into an image-like format, replacing standard RGB-Alpha channels with the four conductance channels. The spatial dimensions represent physical tuning parameters V_{bias} and Γ. By enforcing sparsity along μ, we treat the input as a "bag" of semi-independent 2D images, allowing us to leverage Convolutional Neural Networks (CNNs).

CNNs are exceptionally well-suited for this task due to their reliance on spatial hierarchies and local correlation detection. Experimental signatures of MZMs—such as zero-bias conductance peaks that remain stable over a finite range of Γ, or the closing and reopening of the bulk gap—manifest as continuous, visually distinct local features within this 2D measurement grid. The receptive field of a CNN naturally captures these contiguous physical phase boundaries.

Unlike standard optical images, however, the "pixels" in our input possess strict, absolute physical units. Translation invariance, typically a core strength of CNNs, acts as a fundamental hurdle in this context: a conductance peak centered precisely at $V_{bias} = 0$ carries profound topological implications, whereas an identical peak translated to $V_{bias} = 0.05$ meV represents a physically distinct, likely trivial state. Furthermore, our input is not a contiguous 3D volume, but rather a discontinuous, sparse set of independent slices, requiring specialized architectures to bridge the gaps in the μ parameter space.

2) Model Architecture and Complexity: MEDA employs a modified ResNet-18 shared encoder applied independently to each of the k conductance slices. This provides sufficient depth to learn hierarchical transport features—such as distinguishing a genuine topological gap closing from the crossing of ps-ABS—while remaining lightweight enough to prevent severe overfitting on specific, localized microscopic disorder noise patterns.

To counteract CNN spatial invariance to provide necessary global context, we explicitly inject absolute coordinate values (μ, V_{bias}, Γ) into the latent space via a learned embedding. Following feature extraction, the network utilizes a gated attention pooling mechanism. Because slices near phase transitions provide much more diagnostic utility than those deep in trivial regimes, this layer autonomously weighs each μ slice, filtering out uninformative regions and amplifying critical boundary signatures, aggregating them into a single, unified latent representation.

3) Decoding the PDI: From Classification to Phase Map: Instead of outputting a single device-wide binary label like standard classifiers, MEDA utilizes a CNN decoder—conceptually similar to a U-Net expanding path—to project the aggregated latent representation into a high-resolution 2D spatial grid. While this allows for localized phase predictions, the upsampling process inherently encourages spatial continuity, prioritizing macroscopically stable topological regions over highly fragmented micro-phases. Each pixel $P_{i,j}$ in the predicted phase diagram corresponds to a specific physical configuration (μ_i, Γ_j), with its magnitude representing the uncalibrated probability—or logit—of an operational MZM state.

4) Inherent Challenges and Optimization Drivers: MEDA's architecture targets three physics-induced structural challenges, necessitating the composite loss function detailed in Section III-D:

- **Severe Class Imbalance:** Under realistic disorder, the topologically nontrivial phase space shrinks drastically, biasing standard models toward predicting fully trivial phase diagrams.
- **Phase Fragmentation:** High disorder shatters topological regions into disjointed islands. Unlike standard semantic segmentation tasks that identify highly continuous objects, this fragmentation challenges the network to balance the detection of localized phase boundaries against the risk of fitting to disorder-induced noise.
- **The Missing Data Problem:** Reconstructing a full μ-resolution phase map from sparse μ slices requires highly nonlinear interpolation across wide, unobserved chemical potential gaps.

B. Disorder-Introduced ML Complexity

Realistic, disorder-diverse training data is essential for MEDA to map transport observables to the PDI robustly. In disordered nanowires, transport signatures depend not only on controllable parameters but also on microscopic disorder realizations that are neither directly measurable nor reproducible across devices. To capture this intrinsic variability, we simulate finite nanowire systems over an expanded parameter space that includes both experimentally tunable parameters and latent disorder degrees of freedom, as summarized in Table II.

Disorder Parameters: Realistic modeling of microscopic disorder is central to our problem. Variations in disorder strength V_0, correlation length l_c, and spatial profile lead to substantial modifications of the low-energy spectrum. These variations fragment topological regions, shift phase boundaries, and crucially, produce trivial low-energy states whose nonlocal spectral weights closely masquerade as topological MZMs. To capture this intrinsic topological ambiguity, MEDA adopts a standard disorder model for SM nanowires [51]–[53], [58], parameterized by a site-specific profile $d \in [0, 1]$, overall amplitude V_0, and correlation length l_c.

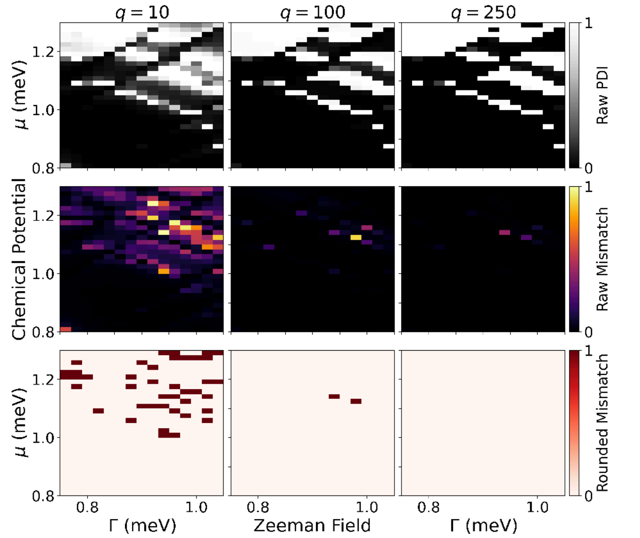

Fig. 4: Top row: Reference raw PDI maps obtained at $q = 10, 100, 250$ iterations for disorder amplitude $V_0 = 1.2$ meV (left to right). Middle row: Difference between the raw PDI maps and the fully converged PDI map computed at $q = 600$ (left to right). Bottom row: Corresponding differences between the rounded PDI value maps and the fully converged PDI maps.

Tunable System Parameters: While the experimentally accessible parameters μ, Γ, and V_{bias} define the measurement space, disorder heavily distorts their relationship to topology. Consequently, transport measurements effectively act as projections of a higher-dimensional, heavily modulated parameter space. We deliberately select broad parameter ranges ($\mu \in [1.5, 3.5]$ meV, $\Gamma \in [0.8, 1.2]$ meV) [51] to force MEDA to learn across regimes where disorder significantly shifts and fragments phase boundaries. MEDA's coverage of the (μ, Γ) parameter space ensures inclusion of regimes where disorder significantly alters phase structure causing conventional indicators to fail. This introduces a unique prediction challenge illustrated in Fig. 5a: unlike more conservative models like ViT [31] that become trivial under heavy disorder, MEDA is explicitly trained to navigate these heavily altered phases, positioning it as a viable tool for real-world MZM detection.

Static System Parameters: Variations in physical mechanisms—such as spectral broadening or Majorana hybridization—can alter the visibility of topological features in transport even when the underlying topology is unchanged. To isolate the effects of disorder while maintaining physically realistic device behavior, we fix static parameters to experimentally relevant values. These include Rashba spin-orbit coupling ($\alpha = 140$ meV) [12], [14], [18], [30], weak and strong SM-SC coupling regimes ($\gamma = 0.2, 0.5$ meV), $\eta = 1 \times 10^{-3}$ meV to model quasiparticle broadening, and system length $L = 3\,\mu$m to balance localization and finite-size effects.

C. High-Fidelity Training Data Synthesis

Transport Observables: Dense multidimensional conductance measurements are the most direct proxy for the sys-

Parameter	Symbol	Observable	Meaning	Values	Granularity
Disorder profile	d	No	Array of point disorders corresponding to each nanowire lattice site	[0, 1]meV	N/A
Global disorder strength	V_0	No	Root mean squared value of the disorder profile	[0.7, 2.5]meV	0.18meV
Correlation length	l_c	No	Characteristic length scale over which disorder potentials exhibit spatial correlations	20, 50, 90 nm	N/A
Chemical potential	μ	Yes	Chemical potential of system	[1.5, 3.5]meV	0.02meV
Bias voltage	V_{bias}	Yes	Voltage difference across nanowire	[-0.05, 0.05]meV	3e-3meV
Zeeman field	Γ	Yes	Effective magnetic field that induces spin splitting in the nanowire	[0.8, 1.2] meV	8e-3meV
SM-SC coupling strength	γ	Yes	Magnitude of superconductor influence on semiconductor nanowire	0.2, 0.5 meV	N/A
Dissipation	η	Yes	Describes the leakage and transmission through the system	0, 1e-3 meV	N/A
System length	L	Yes	Length of the nanowire	3 μm	10nm
Superconducting gap	Δ	Yes	Energy gap of the superconducting parent material	0.3 meV	N/A
RSO coupling strength	α	Yes	Coupling between electron spin and its motion in the nanowire	140meV	N/A

TABLE II: Parameter space for this work. We choose ranges to be representative of real systems. Observability refers to whether a parameter is feasibly measurable/controllable in real systems.

tem's low-energy spectrum, but are severely bottlenecked by experimental measurement time. To train MEDA to operate within these tight constraints, we simulate realistic local and non-local differential conductance using the KWANT quantum transport package [59]. We include an optimal one-site potential barrier at the nanowire-lead interfaces to govern coupling strength, and a finite dissipation term η to capture quasiparticle leakage. The resulting feature space is a four-channel tensor $(G_{LL}, G_{LR}, G_{RL}, G_{RR})$ sampled sparsely across the chemical potential μ.

Ground-Truth PDI Generation: A primary motivation of this work is to circumvent the biases of idealized topological invariants. Therefore, ground-truth labels are synthesized by targeting the disorder-aware PDI [35], which maps the device Hamiltonian to a 1D superlattice formalism to extract the bulk invariant despite strong spatial inhomogeneities. Because this evaluation is highly iterative, calculations are deployed across 191 CPU cores to generate dense phase maps. We enforce a rigorous convergence threshold defined in Fig. 4 to mitigate truncation errors and ensure a stable, binary topological ground truth for optimization.

D. Physics-Guided Optimization

1) Model-Driven μ Slice Selection: As discussed in Section II, dense parameter sweeps are a major bottleneck for experimental studies of Majorana nanowires, especially along the μ axis. MEDA's incorporation of an expanded parameter space to capture shifting topological regimes exacerbates this measurement bottleneck.

MEDA addresses this not by simply subsampling data, but by learning the underlying topological correlations embedded within a highly restricted measurement budget. While our full simulated phase space spans 100 distinct μ-slices, we use attention-pooling mechanism which can extract bulk topological information by correlating non-trivial, fragmented conductance features across non-neighboring μ values [36], [37]. This effectively transforms a dense-scanning infeasibility into a tractable sparse-inference task.

2) Navigating the Topological Loss Landscape: As disorder strength V_0 increases, the topological phase space drastically shrinks and shatters. Standard optimization strategies inevitably collapse in this landscape, falling into a trivial-majority local minimum where the model predicts a uniformly blank phase diagram. To prevent this collapse and force the MEDA to learn the physics of the phase boundaries, we construct a specialized, physically motivated composite loss function $\mathcal{L}$:

$$\mathcal{L}_{total} = \lambda_1 \mathcal{L}_{BCE} + \lambda_2 \mathcal{L}_{Dice} + \lambda_3 \mathcal{L}_{Focal} + \lambda_4 \mathcal{L}_{TV}$$

Binary Cross-Entropy ($\mathcal{L}_{BCE}$) provides the foundational pixel-wise classification gradient, but it is insufficient for resolving fragmented topologies. We therefore integrate Focal Loss ($\mathcal{L}_{Focal}$) to dynamically down-weight the overwhelming trivial majority, forcing the gradient to focus on the rare, hard-to-predict pixels at quantum phase transitions. Dice Loss ($\mathcal{L}_{Dice}$) evaluates spatial overlap, heavily penalizing the model when it misses small, fragmented MZM islands entirely.

Finally, neural networks operating on sparse inputs are prone to generating high-frequency spatial noise: we introduce Total Variation ($\mathcal{L}_{TV}$) regularization to penalize overfragmentation. While this smoothing is essential to prevent the model from hallucinating unrealistic noise artifacts, it introduces a fundamental physical trade-off: MEDA is optimized to identify broader, operationally viable topological regions, which inherently limits its ability to perfectly resolve the highly shattered, microscopic phase boundaries that dominate at extreme disorder strengths. The scalar weights ($\lambda_1 \dots \lambda_4$) act as model hyperparameters, and are optimized via hyperparamter grid search to stabilize the gradient and maintain hypersensitivity to subtle disorder-induced shifts.

(a) PDI maps at low and high V_0 showing the topological region shifts to higher μ and Γ, remaining within the broader parameter space captured by MEDA but well outside the limited ViT window.

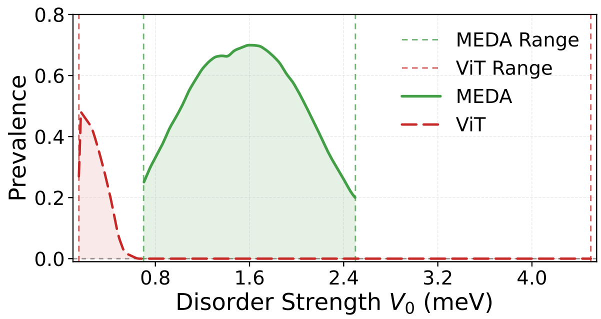

(b) The prevalence of topological activity in ViT's disorder regime quickly converges to zero, while MEDA's regime is optimized to be topologically active.

Fig. 5: While ViT explores a large disorder regime, it is mostly topologically trivial within ViT's limited μ, Γ window. In contrast, MEDA explores a disorder regime and μ, Γ window optimized to capture topological activity.

IV. Evaluation Methodology

A. Evaluation Metrics

MEDA's performance is primarily evaluated using F1 score and precision. The parameter space suffers from severe class imbalance, as trivial phases dominate at higher disorder strengths, V_0. To prevent standard accuracy metrics from being skewed, we use the F1 score for a robust measure of global classification quality. Additionally, we heavily weight precision because false positives—mistaking a trivial state for a topological qubit—are highly detrimental to quantum computing reliability. An effective predictor must maintain both high precision and a strong global F1 score to be viable for real-world devices.

B. Baseline Comparisons

We compare MEDA against two counterparts: (1) the idealized theoretical SMI, which represents the performance oracle and upper limit of SMI-based detection, assuming full knowledge of the system. (2) the ViT framework [31], which is the state-of-the-art learning-based MZM detection using measurements. All comparisons are evaluated relative to the ground-truth PDI. Because the ViT model is closed-source, not available for duplication, we directly cite the results reported in [31], focusing on their full disorder regime spanning $V_0 \in [0.15, 4.5]$ meV. Since ViT predicts a biased SMI map rather than a bulk invariant, we use Bayes' rule to incorporate probabilistic error from SMI biases. As ViT outputs continuous SMI values, we compute the F1 score using a threshold of $\mathrm{SMI} = 0$, following [31].

We note that ViT is trained over a smaller and coarser parameter space, leading to a predominance of trivial SMI maps, particularly at higher disorder strengths. In contrast, MEDA operates over a broader and more finely resolved parameter space, ensuring substantial coverage of regimes containing topological phases, as illustrated in Figs. 5a and 5b. While ViT covers a larger disorder regime than MEDA, Fig. 5b demonstrates that this range is mostly trivial for ViT's parameter window in Fig. 5a. Crucially, while MEDA targets a smaller disorder regime, the entire regime is topologically active, resulting in a larger topologically-nontrivial regime than ViT's.

Furthermore, ViT is trained over a range of correlation lengths $l_c \in [20, 70]$ nm, with l_c randomly sampled for each disorder realization. As correlation length information is not explicitly reported, we compare against models trained at a fixed $l_c = 50$ nm, acknowledging the resulting mismatch. While this training mismatch inherently blurs a purely direct architectural performance delta between MEDA and ViT, we emphasize that MEDA's capacity to learn across a substantially broader and topologically active parameter space establishes it as a more comprehensive tool for real-world phase mapping. Given this training distribution, ViT's predictive performance is expected to degrade at smaller correlation lengths (e.g., $l_c = 20$ nm), where disorder dominates.

C. Evaluation Dataset

Ensuring generalization to realistic devices requires evaluation on disorder realizations that are statistically consistent with, yet distinct from, the training distribution. Accordingly, the evaluation dataset is constructed using the same parameter space defined in Table II, preserving the underlying physical regimes while isolating generalization performance. Since real devices exhibit unique microscopic disorder profiles that cannot be reproduced or controlled, we enforce strict separation between training and evaluation disorder realizations, ensuring that each evaluated system corresponds to a previously unseen disorder configuration. This setup reflects the intrinsic variability of experimental systems and tests the ability of MEDA to learn disorder-robust features rather than memorizing specific realizations.

D. Evaluation Studies

Evaluating MEDA requires quantifying not only predictive accuracy, but also its performance under the intrinsic constraints of disordered, measurement-limited systems. To this end, the evaluation framework is partitioned into four complementary analyses, each probing a distinct aspect of the underlying inverse problem: accuracy relative to theoretical limits, robustness under sparse measurements, interpretability of learned features, and stability across disorder regimes.

1) Global Pipeline Efficacy: We first establish baseline predictive performance relative to both theoretical limits and existing methods. MEDA is evaluated using the global F1 score across 100 unseen disorder profiles at 10 different disorder amplitudes V_0. We compare against the two baselines, quantifying how closely MEDA approaches the SMI limit while improving upon state-of-the-art, thereby establishing MEDA as both theoretically effective and practically competitive.

2) Resolution and Throughput Trade-offs: A central challenge in experimental deployment is the trade-off between measurement sparsity and predictive accuracy. To characterize this, we systematically vary the fraction of available input data during inference. This analysis quantifies the efficiency with which MEDA extracts topological information from incomplete measurements and provides a direct calibration of how predictive accuracy varies as a function of measurement sparsity providing a direct estimate of the performance achievable with a given fraction of the full dataset.

3) Mechanistic Interpretability via Feature Extraction: Given the disorder-induced ambiguity between transport signatures and topology, it is essential to verify that MEDA learns physically meaningful features rather than spurious correlations. To probe this interpretability, we analyze the model's attention weights. By extracting the conductance maps in (Γ, V_{bias}) space that receive the highest attention scores, we can directly compare the model's learned focus against established MZM-indicative transport features, such as those defined by the topological gap protocol (TGP) [40]. This methodology allows us to verify whether MEDA's predictions are grounded in physical reality without providing the model any explicit prior knowledge of these protocols.

4) Robustness in Disordered Regimes: MEDA's robustness against disorder is of significant concern for practical deployment, as guaranteed microscopic inhomogeneities can significantly alter transport signatures without changing the underlying topology. We evaluate MEDA across 100 distinct disorder realizations spanning low, medium, and high correlation regimes $l_c \in \{20, 50, 90\}$ nm, while varying disorder strength over $V_0 \in [0.75, 2.5]$ meV. This analysis maps the operational boundaries of MEDA in the presence of disorder, a critical requirement for translating model predictions into experimentally actionable confidence levels.

V. Results

A. Global Pipeline Quality

MEDA achieves high global predictive quality while operating with only 10% of available data, demonstrating its viability as a measurement-efficient MZM detection pipeline. As shown in Fig. 6, MEDA attains performance comparable to the SMI Oracle—the theoretical ceiling for SMI-based approaches—while outperforming ViT [31], the current state-of-the-art SMI-based pipeline, despite targeting a more complex parameter space.

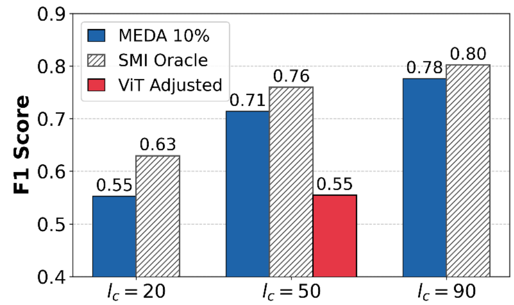

Fig. 6: Despite using only 10% of observable data, MEDA achieves performance comparable to the SMI Oracle (computed with unobtainable full system information) and offers significant improvement over ViT, the state-of-the-art SMI-based prediction pipeline.

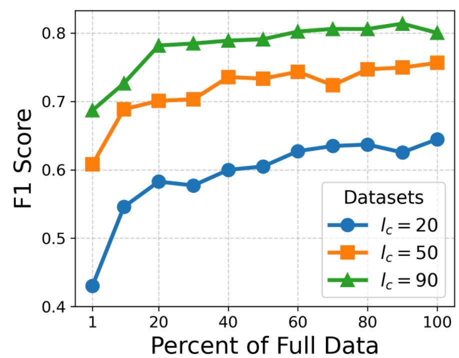

Fig. 7: F1 Score vs Data Usage, with training limited to 500 epochs. Notice that past 10% of full data, increasing data has diminishing returns.

MEDA's performance exhibits a clear dependence on disorder correlation length, reflecting its disorder-aware design. The gap between MEDA and the SMI Oracle is largest at low $l_c = 20$, where highly jagged disorder profiles produce less predictable transport signatures. As l_c increases, smoother disorder leads to more stable topological features and correspondingly improved predictive accuracy.

B. Resolution and Throughput Tradeoffs

MEDA enables a tunable trade-off between measurement cost and predictive accuracy, directly addressing experimental data acquisition constraints. Fig. 7 shows a logarithmic relationship between the fraction of input data used during inference and the resulting F1 score. While MEDA operates at 10% input data to significantly reduce measurement burden, the framework allows flexible adjustment depending on experimental requirements.

The performance curve reveals diminishing returns beyond modest data fractions, validating MEDA's measurement-efficient design. In particular, systems with $l_c = 90$ maintain high F1 scores with as little as 1% of full conductance data, indicating that accurate topological inference can be achieved with extremely sparse measurements. This suggests the potential for near real-time analysis of MZM systems under favorable disorder conditions.

For subsequent evaluations, we fix the input fraction at 10% to reflect a practically achievable measurement regime. As we will demonstrate in our throughput analysis, this specific fraction provides an optimal trade-off, maximizing experimental viability while preventing the diminishing returns observed at denser sampling rates. This choice prioritizes practicality for real-world systems while maintaining strong predictive performance.

C. Physics-Informed Feature Extraction

MEDA learns physically meaningful features by selectively prioritizing informative chemical potential slices, demonstrating that the model identifies topological signatures directly from conductance data rather than relying on spurious correlations. Fig. 8 shows an illustrative example of a single μ-slice conductance profile set, selected from the conductance slices with the highest 0.01% of attention scores across the entire evaluation dataset.

The selected high-attention conductance profiles exhibit clear signatures consistent with the topological gap protocol (TGP), including zero-bias peaks in local conductance channels and gap closing and reopening features in non-local conductance channels. Importantly, this behavior emerges without any explicit encoding of TGP-based criteria in the model, indicating that MEDA autonomously learns to identify physically meaningful topological features. This constitutes, to our knowledge, the first instance of a model demonstrating the ability to prioritize embedded topological information aligned with established experimental protocols without any protocol-specific training.

These results demonstrate that MEDA's feature selection mechanism is grounded in physically interpretable transport signatures, enabling targeted identification of high-information regions in parameter space. By demonstrating this capability, MEDA provides a principled foundation for designing measurement strategies that prioritize informative μ slices over uniform sampling.

D. Robustness in Disordered Regimes

MEDA maintains strong predictive performance across varying disorder strengths, establishing its reliability in realistic nanowire environments. While performance degrades with increasing disorder strength V_0, MEDA consistently remains competitive as a practical MZM detection method. We note that all results in this section are obtained under a fixed measurement constraint of 10% input data. As demonstrated in Fig. 7, increasing the available data fraction leads to systematic improvements in predictive accuracy, indicating that the observed degradation at higher V_0 and lower l_c primarily reflects measurement sparsity rather than a fundamental limitation of the framework.

1) Low Disorder-Correlation Regime $l_c = 20nm$: The low disorder-correlation regime represents the most challenging setting for disorder-aware prediction due to highly jagged disorder profiles. As shown in Fig. 9, MEDA achieves lower baseline F1 scores in this regime, with performance degrading more rapidly as V_0 increases. Nevertheless, MEDA retains useful predictive capability into moderate disorder strengths.

SMI also shows reduced effectiveness in this regime, reflecting its lack of disorder awareness. Jagged disorder profiles amplify discrepancies between disorder-aware and disorder-unaware diagnostics, limiting SMI's reliability.

ViT is expected to show limited sensitivity to increasing disorder in this regime due to its restricted parameter window. Because its predictions collapse into predominantly trivial classifications at higher disorder, its F1 score flattens out, reflecting a complete loss of predictive sensitivity rather than robustness. If evaluated over the broader parameter space used by MEDA, a similar degradation trend would likely emerge.

2) Medium Disorder-Correlation Regime $l_c = 50nm$: In the medium disorder-correlation regime, MEDA achieves performance comparable to SMI across a broad range of disorder strengths, demonstrating its effectiveness in experimentally relevant conditions. While SMI serves as a useful reference, its reliance on inaccessible full-system information limits its direct applicability. In contrast, MEDA's comparable performance, combined with its reliance on experimentally accessible inputs, positions it as a practical methodology for real-world MZM detection. MEDA is particularly well positioned compared to widely-used SMI-based pipelines, which compound prediction errors with errors inherent in their SMI target.

3) High Disorder-Correlation Regime $l_c = 90nm$: MEDA achieves its strongest performance in high disorder-correlation regimes, where smoother disorder profiles preserve topological structure. As shown in Fig. 11, MEDA remains more stable with increasing disorder strength V_0 compared to lower l_c regimes. The improved performance reflects the increased stability of transport signatures under smoother disorder, allowing MEDA's feature extraction to operate with higher confidence. This trend confirms that disorder correlation length is a key factor governing predictive reliability.

Importantly, MEDA can exceed SMI performance in certain low-disorder regimes within this setting. Because the SMI is fundamentally boundary-focused and susceptible to quasi-Majorana false positives, MEDA's disorder-aware, bulk-oriented mapping provides a more accurate reflection of the true PDI ground truth. This result highlights the limitations of relying on boundary-based invariants in realistic systems.

E. Qualitative Analysis

While MEDA exhibits strong predictive performance relative to existing work, it remains challenged by heavy fragmentation and chaotic topological phase boundaries. Fig. 12 shows that MEDA over-prioritizes smooth phase boundaries and consistent regions, resulting in erroneously simplified predictions of highly fragmented landscapes.

We attribute MEDA's tendency to oversimplify landscapes to our extensive optimization against overfitting. Because each real-world system is guaranteed a unique disorder profile, it

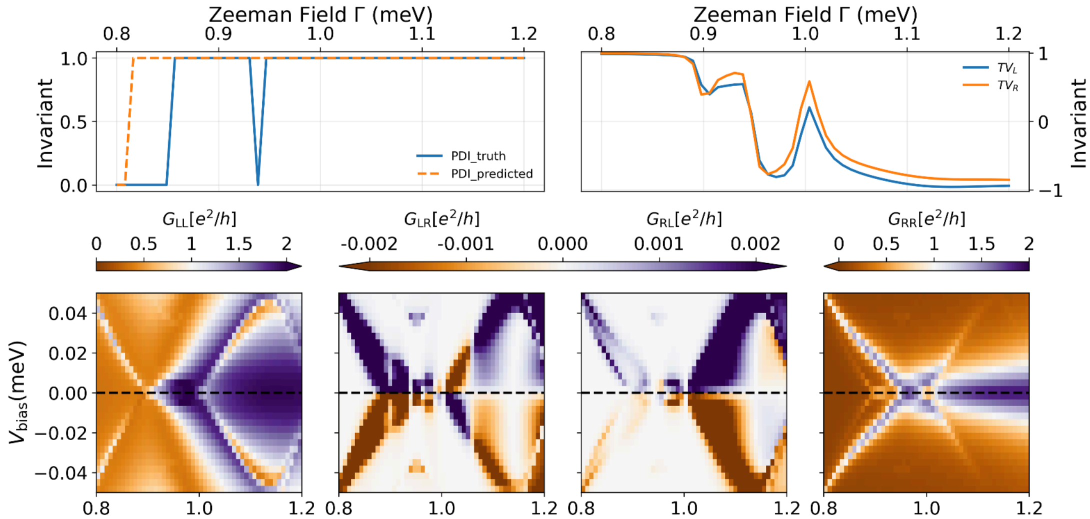

Fig. 8: MEDA's trained attention weights heavily prioritize this conductance map with clearly visible conductance features that Morteza et al. establish as indicators of high topological phase probability [40]. As far as we are aware, MEDA is the first machine learning approach to demonstrably learn physical MZM-heralding features without any training or guidance specifying those features.

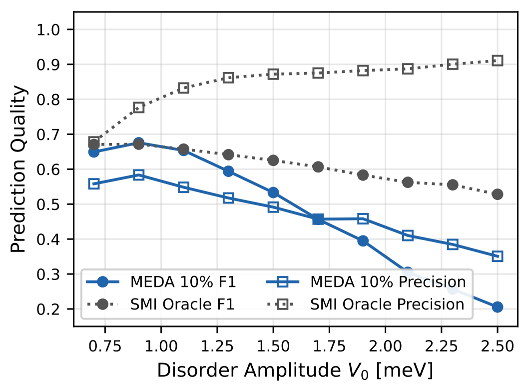

Fig. 9: In the low disorder-correlation regime ($l_c = 20nm$), MEDA performs well for lower V_0 disorder, but struggles at higher V_0 due to significant fragmentation and more-pronounced class imbalance.

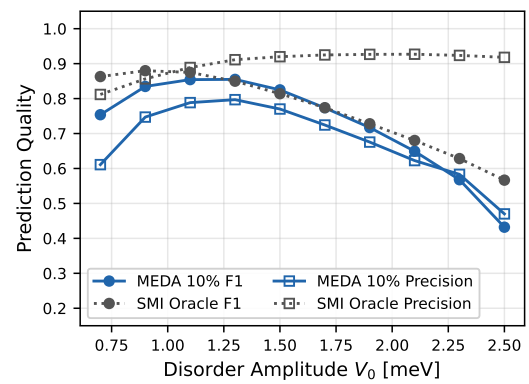

Fig. 11: In the high disorder-correlation regime ($l_c = 90$nm) smoother disorder profiles allow MEDA to retain high predictive accuracy even at elevated disorder strengths.

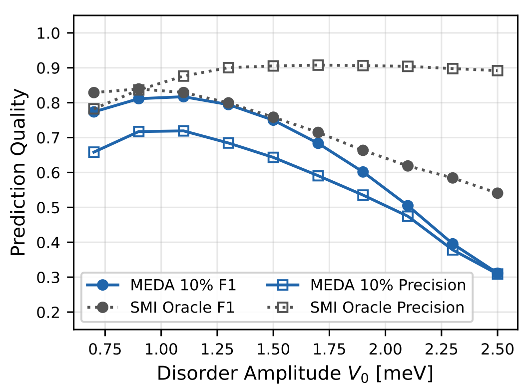

Fig. 10: MEDA maintains predictive performance comparable to the theoretical SMI baseline up until high disorder (V_0) levels in the medium disorder-correlation regime ($l_c = 50$nm), highlighting its viability as an indicator for real-world devices.

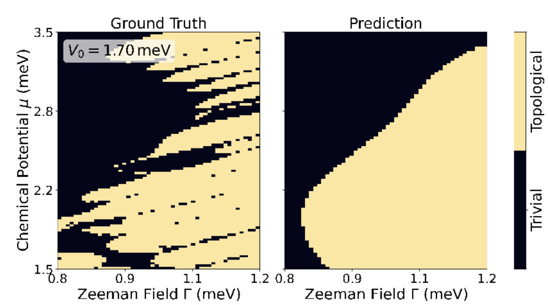

Fig. 12: MEDA predicts smooth topological phase transitions and continuous regions. While this helps to avoid overfitting during training, it leads to misclassifications for heavily fragmented topological phases under high disorder.

is essential to avoid overfitting to the training dataset. Many overfit-prevention techniques—including MEDA's training input noise injection and total variation regularization—actively encourage smoother prediction maps that may not accurately represent the highly-fragmented topological phase maps at high disorder. Significant analysis is required to uncover the optimal balance between overfit prevention and fragmentation prediction; we leave this to future work.

VI. Related Work

MEDA is an end-to-end framework designed to predict MZMs in real-world, 1D nanowire devices. We situate MEDA's contributions relative to three prevailing paradigms of MZM detection: idealized theoretical indicators, hardware-driven experimental diagnostics, and recent data-driven machine learning frameworks.

A. Theoretical and Experimental Diagnostics

Foundational theoretical models establish the basis for MZMs through bulk invariants and gap-closing signatures [5], [7]–[10]. However, as detailed in Section II, attempting to adapt these concepts into finite-system indicators—such as the SMI [11], [33], [54], [55] or local density of states [51]–[53]—results in boundary-induced biases and severe false positives in the presence of disorder. On the experimental front, hardware validation relies heavily on tunneling spectroscopy [12]–[14], [18], [19], [32], [39] and advanced correlation methods like the TGP [25], [60]. While these experimental approaches provide and validate necessary transport observables, they face severe measurement scalability bottlenecks and interpretability challenges when attempting to construct global phase diagrams.

B. Machine Learning in MZM Detection

Recent literature has increasingly turned to machine learning to connect theoretical indicators and experimental observables. Cheng et al. demonstrated that ML models can successfully extract disorder-dependent topological information from conductance data [37]. Similarly, Taylor and Sarma deployed a Vision Transformer architecture to reproduce SMI directly from conductance maps [31]. Other data-driven frameworks aim to infer underlying disorder characteristics from transport measurements [36].

C. MEDA's Novelty and Contrast

While these ML approaches represent a significant step forward, they remain fundamentally limited by two constraints: topological bias and measurement scalability. Because existing models predominantly target the SMI, their predictions inherently inherit its boundary-related biases, resulting in the incorrect classification of quasi-Majorana states and phases obscured by finite-size effects. Furthermore, these architectures rely on dense conductance maps, failing to account for the prohibitively high serial measurement cost of sweeping the chemical potential in laboratory settings.

MEDA distinguishes itself from other works relating observables to invariants in two critical ways.

1) **Targeting an Unbiased Ground Truth:** To our knowledge, MEDA is the first ML framework that eliminates boundary-induces biases by targeting the bulk-defined, disorder-aware PDI [35], providing resiliency against quasi-Majorana states and finite-size effects.
2) **Measurement-Efficient Inference:** Rather than requiring dense parameter sweeps, MEDA utilizes deliberately sparse conductance data. By explicitly learning to prioritize high-information chemical potential slices——autonomously extracting features consistent with established experimental criteria like the TGP——MEDA provides a practical pathway for identifying topological regimes with a $10\times$ reduction in experimental overhead.

VII. Conclusion

In this work, we present present MEDA, a measurement-efficient framework for the robust detection of MZMs in finite, disordered systems. By directly mapping experimentally accessible transport observables to the disorder-aware PDI, MEDA successfully avoids the boundary-induced biases and false positives inherent to conventional indicators like the SMI.

Crucially, MEDA overcomes the severe serial data acquisition bottleneck that currently limits experimental scalability. Using an attention-based architecture to aggregate sparse conductance measurements, the model achieves up to a $10\times$ reduction in required input data with minimal loss in predictive accuracy. MEDA remains robust even under strong disorder and finite-size effects where traditional indicators fail, providing a highly scalable and practical pathway for mapping topological phase boundaries in realistic devices.

While MEDA represents a significant advance in scalable MZM detection, certain limitations remain. Specifically, the strong regularization required to prevent overfitting to unique disorder profiles currently leads the model to oversimplify highly fragmented topological landscapes at extreme disorder strengths. Future works must determine a more optimal balance between noise suppression and high-resolution phase boundary prediction. Potential methodologies may include adaptive regularization schemes that dynamically scale the $\mathcal{L}_{TV}$ penalty in response to high local variance, or alternative loss functions that penalize phase boundary mismatches without aggressively smoothing localized topological islands. Moving forward, the physical interpretability of MEDA's attention mechanism offers broader implications beyond static classification; the features prioritized by the model could inform the design of more resilient nanowire architectures or eventually guide adaptive data acquisition. Ultimately, MEDA establishes a robust, measurement-efficient foundation for translating theoretical topological invariants into practical experimental diagnostics.

References

[1] C. Nayak and F. Wilczek, "2n-quasihole states realize 2^{n-1}-dimensional spinor braiding statistics in paired quantum hall states," *Nucl. Phys. B*, vol. 479, no. 3, pp. 529–553, 1996.

[2] N. Read and D. Green, "Paired states of fermions in two dimensions with breaking of parity and time-reversal symmetries and the fractional quantum hall effect," *Phys. Rev. B*, vol. 61, pp. 10 267–10 297, Apr 2000. [Online]. Available: https://link.aps.org/doi/10.1103/PhysRevB.61.10267
[3] G. Moore and N. Read, "Nonabelions in the fractional quantum Hall effect," *Nucl. Phys. B*, vol. 360, no. 2–3, pp. 362–396, 1991.
[4] C. Nayak, S. H. Simon, A. Stern, M. Freedman, and S. Das Sarma, "Non-abelian anyons and topological quantum computation," *Rev. Mod. Phys.*, vol. 80, pp. 1083–1159, Sep 2008. [Online]. Available: https://link.aps.org/doi/10.1103/RevModPhys.80.1083
[5] A. Y. Kitaev, "Fault-tolerant quantum computation by anyons," *Ann. Phys.*, vol. 303, no. 1, pp. 2–30, 2003.
[6] F. Wilczek, "Quantum mechanics of fractional-spin particles," *Phys. Rev. Lett.*, vol. 49, no. 14, p. 957, 1982.
[7] R. M. Lutchyn, J. D. Sau, and S. D. Sarma, "Majorana fermions and a topological phase transition in semiconductor-superconductor heterostructures," *Phys. Rev. Lett.*, vol. 105, no. 7, p. 077001, 2010.
[8] Y. Oreg, G. Refael, and F. von Oppen, "Helical liquids and majorana bound states in quantum wires," *Phys. Rev. Lett.*, vol. 105, no. 17, p. 177002, 2010.
[9] J. D. Sau, S. Tewari, R. M. Lutchyn, T. D. Stanescu, and S. D. Sarma, "Non-abelian quantum order in spin-orbit-coupled semiconductors: Search for topological majorana particles in solid-state systems," *Phys. Rev. B*, vol. 82, no. 21, p. 214509, 2010.
[10] J. D. Sau, R. M. Lutchyn, S. Tewari, and S. D. Sarma, "Generic new platform for topological quantum computation using semiconductor heterostructures," *Phys. Rev. Lett.*, vol. 104, no. 4, p. 040502, 2010.
[11] I. A. Day, A. L. R. Manesco, M. Wimmer, and A. R. Akhmerov, "Identifying biases of the Majorana scattering invariant," *SciPost Phys. Core*, vol. 8, p. 047, 2025. [Online]. Available: https://scipost.org/10.21468/SciPostPhysCore.8.3.047
[12] V. Mourik, K. Zuo, S. M. Frolov, S. Plissard, E. P. Bakkers, and L. P. Kouwenhoven, "Signatures of majorana fermions in hybrid superconductor-semiconductor nanowire devices," *Sci.*, vol. 336, no. 6084, pp. 1003–1007, 2012.
[13] M. T. Deng, C. L. Yu, G. Y. Huang, M. Larsson, P. Caroff, and H. Q. Xu, "Anomalous zero-bias conductance peak in a nb–insb nanowire–nb hybrid device," *Nano. Lett.*, vol. 12, no. 12, pp. 6414–6419, Dec 2012. [Online]. Available: https://doi.org/10.1021/nl303758w
[14] A. Das, Y. Ronen, Y. Most, Y. Oreg, M. Heiblum, and H. Shtrikman, "Zero-bias peaks and splitting in an al–inas nanowire topological superconductor as a signature of majorana fermions," *Nat. Phys.*, vol. 8, no. 12, pp. 887–895, Dec 2012. [Online]. Available: https://doi.org/10.1038/nphys2479
[15] L. P. Rokhinson, X. Liu, and J. K. Furdyna, "The fractional ac josephson effect in a semiconductor–superconductor nanowire as a signature of majorana particles," *Nat. Phys.*, vol. 8, no. 11, p. 795, 2012.
[16] H. e. a. Churchill, "Superconductor-nanowire devices from tunneling to the multichannel regime: Zero-bias oscillations and magnetoconductance crossover," *Phys. Rev. B*, vol. 87, no. 24, p. 241401, 2013.
[17] A. Finck, D. J. Van Harlingen, P. Mohseni, K. Jung, and X. Li, "Anomalous modulation of a zero-bias peak in a hybrid nanowire-superconductor device," *Phys. Rev. Lett.*, vol. 110, no. 12, p. 126406, 2013.
[18] M. e. a. Deng, "Majorana bound state in a coupled quantum-dot hybrid-nanowire system," *Sci.*, vol. 354, no. 6319, pp. 1557–1562, 2016.
[19] H. e. a. Zhang, "Ballistic superconductivity in semiconductor nanowires," *Nat. Comm.*, vol. 8, p. 16025, 2017.
[20] J. e. a. Chen, "Experimental phase diagram of zero-bias conductance peaks in superconductor/semiconductor nanowire devices," *Sci. Adv.*, vol. 3, no. 9, p. e1701476, 2017.
[21] F. e. a. Nichele, "Scaling of majorana zero-bias conductance peaks," *Phys. Rev. Lett.*, vol. 119, no. 13, p. 136803, 2017.
[22] S. Mi, D. I. Pikulin, M. Marciani, and C. W. J. Beenakker, "X-shaped and y-shaped andreev resonance profiles in a superconducting quantum dot," *J. Exp. Theor. Phys.*, vol. 119, no. 6, pp. 1018–1027, Dec 2014. [Online]. Available: https://doi.org/10.1134/S1063776114120176
[23] D. Bagrets and A. Altland, "Class d spectral peak in majorana quantum wires," *Phys. Rev. Lett.*, vol. 109, no. 22, p. 227005, 2012.
[24] D. I. Pikulin, J. Dahlhaus, M. Wimmer, H. Schomerus, and C. Beenakker, "A zero-voltage conductance peak from weak antilocalization in a majorana nanowire," *New J. Phys.*, vol. 14, no. 12, p. 125011, 2012.
[25] E. Prada, P. San-Jose, and R. Aguado, "Transport spectroscopy of n s nanowire junctions with majorana fermions," *Phys. Rev. B*, vol. 86, no. 18, p. 180503, 2012.
[26] H. Pan and S. D. Sarma, "Physical mechanisms for zero-bias conductance peaks in majorana nanowires," *Phys. Rev. Res.*, vol. 2, no. 1, p. 013377, 2020.
[27] C. Moore, T. D. Stanescu, and S. Tewari, "Two-terminal charge tunneling: Disentangling majorana zero modes from partially separated andreev bound states in semiconductor-superconductor heterostructures," *Phys. Rev. B*, vol. 97, no. 16, p. 165302, 2018.
[28] C. Moore, C. Zeng, T. D. Stanescu, and S. Tewari, "Quantized zero-bias conductance plateau in semiconductor-superconductor heterostructures without topological majorana zero modes," *Phys. Rev. B*, vol. 98, p. 155314, Oct 2018. [Online]. Available: https://link.aps.org/doi/10.1103/PhysRevB.98.155314
[29] A. Vuik, B. Nijholt, A. R. Akhmerov, and M. Wimmer, "Reproducing topological properties with quasi-Majorana states," *SciPost Phys.*, vol. 7, p. 061, 2019.
[30] T. D. Stanescu and S. Tewari, "Robust low-energy andreev bound states in semiconductor-superconductor structures: Importance of partial separation of component majorana bound states," *Phys. Rev. B*, vol. 100, no. 15, p. 155429, 2019.
[31] J. R. Taylor and S. Das Sarma, "Vision transformer based deep learning of topological indicators in majorana nanowires," *Phys. Rev. B*, vol. 111, p. 104208, Mar 2025. [Online]. Available: https://link.aps.org/doi/10.1103/PhysRevB.111.104208
[32] A. R. Akhmerov, J. P. Dahlhaus, F. Hassler, M. Wimmer, and C. W. J. Beenakker, "Quantized conductance at the majorana phase transition in a disordered superconducting wire," *Phys. Rev. Lett.*, vol. 106, p. 057001, 2011.
[33] I. C. Fulga, F. Hassler, and A. R. Akhmerov, "Scattering theory of topological insulators and superconductors," *Phys. Rev. B*, vol. 85, p. 165409, 2012.
[34] S. Das Sarma, A. Nag, and J. D. Sau, "How to infer non-abelian statistics and topological visibility from tunneling conductance properties of realistic majorana nanowires," *Phys. Rev. B*, vol. 94, p. 035143, 2016.
[35] R. Eissele, B. B. Roy, S. Tewari, and T. D. Stanescu, "Topological invariant for finite systems in the presence of disorder," 2025. [Online]. Available: https://arxiv.org/abs/2508.13146
[36] J. R. Taylor, J. D. Sau, and S. Das Sarma, "Machine learning the disorder landscape of majorana nanowires," *Phys. Rev. Lett.*, vol. 132, p. 206602, May 2024. [Online]. Available: https://link.aps.org/doi/10.1103/PhysRevLett.132.206602
[37] M. Cheng, R. Okabe, A. Chotrattanapituk, and M. Li, "Machine learning detection of majorana zero modes from zero-bias peak measurements," *Matter*, vol. 7, no. 7, pp. 2507–2520, 2024. [Online]. Available: https://www.sciencedirect.com/science/article/pii/S2590238524002534
[38] Ö. e. a. Gül, "Ballistic majorana nanowire devices," *Nat. Nano.*, vol. 13, no. 3, pp. 192–197, 2018.
[39] S. M. e. a. Albrecht, "Exponential protection of zero modes in majorana islands," *Nat.*, vol. 531, no. 7593, pp. 206–209, 2016.
[40] M. e. a. Aghaee, "Inas-al hybrid devices passing the topological gap protocol," *Phys. Rev. B*, vol. 107, p. 245423, Jun 2023. [Online]. Available: https://link.aps.org/doi/10.1103/PhysRevB.107.245423
[41] T. A. Baart, P. T. Eendebak, C. Reichl, W. Wegscheider, and L. M. K. Vandersypen, "Computer-automated tuning of semiconductor double quantum dots into the single-electron regime," *Appl. Phys. Lett.*, vol. 108, no. 21, May 2016. [Online]. Available: http://dx.doi.org/10.1063/1.4952624
[42] J. e. a. Darulová, "Autonomous tuning and charge-state detection of gate-defined quantum dots," *Phys. Rev. Appl.*, vol. 13, no. 5, May 2020. [Online]. Available: http://dx.doi.org/10.1103/PhysRevApplied.13.054005
[43] S. e. a. Albrecht, "Transport signatures of quasiparticle poisoning in a majorana island," *Phys. Rev. Lett.*, vol. 118, no. 13, p. 137701, 2017.
[44] E. e. a. O Farrell, "Hybridization of subgap states in one-dimensional superconductor-semiconductor coulomb islands," *Phys. Rev. Lett.*, vol. 121, no. 25, p. 256803, 2018.
[45] J. e. a. Shen, "Parity transitions in the superconducting ground state of hybrid insb–al coulomb islands," *Nat. Comm.*, vol. 9, no. 1, p. 4801, 2018.
[46] D. Sherman, J. Yodh, S. M. Albrecht, J. Nygård, P. Krogstrup, and C. M. Marcus, "Normal, superconducting and topological regimes of hybrid double quantum dots," *Nat. Nano.*, vol. 12, no. 3, p. 212, 2017.

[47] S. e. a. Vaitiekėnas, "Selective-area-grown semiconductor-superconductor hybrids: A basis for topological networks," *Phys. Rev. Lett.*, vol. 121, no. 14, p. 147701, 2018.
[48] P. e. a. Yu, "Non-majorana states yield nearly quantized conductance in proximatized nanowires," *Nat. Phys.*, vol. 17, no. 4, p. 482–488, Jan 2021. [Online]. Available: http://dx.doi.org/10.1038/s41567-020-01107-w
[49] H. Z. et al., "Large zero-bias peaks in insb-al hybrid semiconductor-superconductor nanowire devices," 2021.
[50] G. Kells, D. Meidan, and P. Brouwer, "Near-zero-energy end states in topologically trivial spin-orbit coupled superconducting nanowires with a smooth confinement," *Phys. Rev. B*, vol. 86, no. 10, p. 100503, 2012.
[51] B. B. Roy, R. Jaiswal, T. D. Stanescu, and S. Tewari, "Stabilizing topological superconductivity in disordered spin-orbit coupled semiconductor-superconductor heterostructures," *Phys. Rev. B*, vol. 110, p. 115436, Sep 2024. [Online]. Available: https://link.aps.org/doi/10.1103/PhysRevB.110.115436
[52] T. D. Stanescu and S. Tewari, "Majorana fermions in semiconductor nanowires: fundamentals, modeling, and experiment," *J. Phys. Cond. Matt.*, vol. 25, no. 23, p. 233201, May 2013. [Online]. Available: http://dx.doi.org/10.1088/0953-8984/25/23/233201
[53] T. D. Stanescu, S. Tewari, J. D. Sau, and S. Das Sarma, "To close or not to close: The fate of the superconducting gap across the topological quantum phase transition in majorana-carrying semiconductor nanowires," *Phys. Rev. Lett.*, vol. 109, p. 266402, Dec 2012. [Online]. Available: https://link.aps.org/doi/10.1103/PhysRevLett.109.266402
[54] I. C. Fulga, F. Hassler, A. R. Akhmerov, and C. W. J. Beenakker, "Scattering formula for the topological quantum number of a disordered multimode wire," *Phys. Rev. B*, vol. 83, p. 155429, Apr 2011. [Online]. Available: https://link.aps.org/doi/10.1103/PhysRevB.83.155429
[55] D. I. P. et al., "Protocol to identify a topological superconducting phase in a three-terminal device," 2021. [Online]. Available: https://arxiv.org/abs/2103.12217
[56] A. Vuik, B. Nijholt, A. R. Akhmerov, and M. Wimmer, "Reproducing topological properties with quasi-majorana states," *arXiv*, 2018.
[57] J.-Y. Wang, N. van Loo, G. P. Mazur, V. Levajac, F. K. Malinowski, M. Lemang, F. Borsoi, G. Badawy, S. Gazibegovic, E. P. A. M. Bakkers, M. Quintero-Pérez, S. Heedt, and L. P. Kouwenhoven, "Parametric exploration of zero-energy modes in three-terminal insb-al nanowire devices," *Phys. Rev. B*, vol. 106, p. 075306, Aug 2022. [Online]. Available: https://link.aps.org/doi/10.1103/PhysRevB.106.075306
[58] J. D. Sau and S. Das Sarma, "Density of states of disordered topological superconductor-semiconductor hybrid nanowires," *Phys. Rev. B*, vol. 88, no. 6, Aug. 2013. [Online]. Available: http://dx.doi.org/10.1103/PhysRevB.88.064506
[59] C. W. Groth, M. Wimmer, A. R. Akhmerov, and X. Waintal, "Kwant: a software package for quantum transport," *New J. Phys.*, vol. 16, no. 6, p. 063065, Jun. 2014. [Online]. Available: http://dx.doi.org/10.1088/1367-2630/16/6/063065
[60] H. Z. et al., "Quantized majorana conductance," *Nat.*, vol. 556, pp. 74–79, 2018.